Geophys. J. Int. (2005) **163,** 357–371 doi: 10.1111/j.1365-246X.2005.02645.x

Modelling post-glacial rebound with lateral viscosity variations

Archie Paulson, Shijie Zhong and John Wahr*

Department of Physics, University of Colorado, Boulder, CO, 80309, *USA. E-mail: archie.paulson@colorado.edu*

Accepted 2005 March 17. Received 2005 February 24; in original form 2004 November 10

SUMMARY

Observations of isostatic adjustment of the Earth's surface due to glacial loading provide important constraints on mantle viscosity structure. We solve the forward problem of glacial isostatic adjustment in two complementary ways: a spectral method for strictly 1-D (spherically symmetric) earth models, and a finite element method that can accommodate 3-D viscosity structure. We discuss how each method may be augmented in three ways: to accommodate motion of the centre of mass, to implement a gravitationally self-consistent ocean load via the sea level equation and to include the influence of polar wander. With all these effects implemented, the two methods are benchmarked against each other. We also study the influence of lateral viscosity variations upon measurements of post-glacial rebound (PGR) in two ways: first by observing the effect of viscosity perturbations in an idealized model and second by developing a realistic 3-D viscosity model and comparing it with results of related 1-D (spherically symmetric) models. The 3-D viscosity structure is derived starting from seismic tomography models. We conclude from both approaches that PGR observations are sensitive to both the local viscosity structure and to the viscosity structure beneath the loaded region, even if it is removed from where the observations are made. In particular, PGR measurements made at Hudson Bay tend to reflect the local viscosity structure beneath Hudson Bay; PGR measurements made along the east coast of North America, being sensitive to both the local (east coast) viscosity structure as well as the loaded (continental) viscosity structure, are not reproducible with a 1-D viscosity model.

Key words: glacial rebound, lateral heterogeneity, mantle viscosity, polar motion, viscoelasticity.

1 INTRODUCTION

Important constraints on mantle viscosity can be made by comparing observations of post-glacial rebound (PGR) with model predictions of the Earth's response to deglaciation. Due to the demands of PGR modelling, however, most studies have been restricted to the inference of only 1-D, radially stratified viscosity structure. Yet we know that lateral variations may be important. Solution for viscoelastic deformation has recently become possible on earth models with a fully 3-D structure (e.g. Kaufmann *et al.* 2000; Martinec *et al.* 2001; Zhong *et al.* 2003). Though we may now solve the forward problem given a certain viscosity structure and loading history, two important problems remain: including in the model realistic and significant complicating effects (such as a gravitationally responsive ocean load and polar wander feedback) and considering the influence of 3-D viscosity variations on the 1-D inverse problem (the inference of 1-D viscosity structure from PGR observations).

This paper is structured to meet two distinct goals. One is to thoroughly describe the implementation of three effects that make the PGR modelling more realistic. These effects are: (1) solution of the Earth's response at spherical harmonic degree one (or, equivalently, accommodation of motion of the Earth's centre of mass); (2) application of an ocean load that conserves the mass in the ice sheets and responds to the evolving topography and geoid; (3) interaction between motion of the Earth's rotational pole and deformation via changes to centrifugal potential. Previous work has considered the implementation of the sea level equation (e.g. Milne *et al.* 1999; Wu & van der Wal 2003) and the influence polar wander on deformation (e.g. Han & Wahr 1989; Mitrovica *et al.* 2005). Considering the significant influence of these effects and their mutual interaction, demonstrated below, a comprehensive PGR model should include all of them. We present the implementation of each of these effects separately in two solution methods: a 3-D finite-element method and a more traditional spectral method.

The second goal is to use our finite-element code to compute the response of an Earth with fully 3-D viscosity variations. Most studies concerning the inference of mantle viscosity from PGR measurements are restricted to 1-D, radially stratified models. We are motivated by the following question: when a 1-D viscosity model is

*Also at: Cooperative Institute for Research in Environmental Sciences, University of Colorado Boulder, CO, USA.

derived from PGR observations, how does this viscosity structure correspond to the 3-D structure of the Earth? For example, if sea level measurements along a continental coast can tell us about the mantle viscosity, would it give simply the viscosity beneath the point of measurement or be influenced by viscosity structure in other regions? Would lateral viscosity variations complicate the inference of a 1-D viscosity model? Since running a 3-D forward model is computationally demanding, and since a 3-D structure has far too many degrees of freedom, we cannot hope to attempt an inversion for 3-D viscosity structure from PGR data. Instead, in this paper we study the influence of 3-D viscosity variations in two ways. First, in Section 3.3, we study the influence of viscosity perturbations in an idealized model. We map a 'sensitivity region' in the mantle where viscosity perturbations can affect surface deformation. Second, in Section 3.4, we measure the PGR observables resulting from a realistic 3-D viscosity structure that is derived from seismic tomography models. We then compare the PGR observations with those computed from 1-D (spherically symmetric) models, whose viscosity is derived from the 3-D model. We investigate different methods of deriving a 1-D average viscosity from the 3-D structure, seeking to best reproduce the PGR observations from the 3-D model. If an optimal method exists, it could be used to describe how 1-D viscosity structures, derived from actual PGR observations, relate to the true 3-D viscosity of the Earth.

2 MODEL FORMULATION AND SOLUTION PROCEDURES

2.1 Physical model

Our models of viscoelastic deformation assume an incompressible, self-gravitating Earth. The mantle is treated as a viscoelastic solid overlying an inviscid core. We solve the governing equations of mass and momentum conservation, along with gravitational perturbation via Poisson's equation (Wu & Peltier 1982):

$$u_{i,i} = 0, \tag{1}$$

$$\sigma_{ij,j} + \rho_0 \phi_{,i} - \rho_1 g_i - (\rho_0 g u_r)_{,i} = 0, \tag{2}$$

$$\phi_{,ii} = -4\pi G \rho_1, \tag{3}$$

where the notation $A_{,i}$ represents differentiation of A with respect to coordinate x_i (in a coordinate system with origin at the centre of figure of the unperturbed Earth), u_i is the displacement (u_r its radial component), σ_{ij} is the stress tensor, ρ_0 and ρ_1 are the unperturbed density and Eulerian density ($\rho_1 = -u_i \rho_{0,i}$), g_i is the gravitational acceleration, ϕ is the perturbation of the gravitational potential and G is the gravitational constant. In this study we consider only uniform mantle density, $\rho_0 =$ constant, so the Eulerian density perturbation ρ_1 vanishes from eqs (2) and (3).

The boundary condition at the core–mantle boundary (CMB) is determined by the continuity of normal stress across the boundary. Eq. (2) for the fluid core, with $\sigma_{ij} = -P\delta_{ij}$ (where P is pressure) gives

$$\sigma_{ij} n_j = (\rho_c \phi - u_r \rho_c g) n_i \qquad \text{for} \qquad r = r_b, \tag{4}$$

where ρ_c is the core density (constant throughout the core), r_b is the core radius and n_i is a vector normal to the boundary (pointing away from the core). The boundary condition at the surface is determined by the ocean and ice loads:

$$\sigma_{ij} n_j = -\sigma_{app}(\theta, \varphi, t) n_i \qquad \text{for} \qquad r = r_s, \tag{5}$$

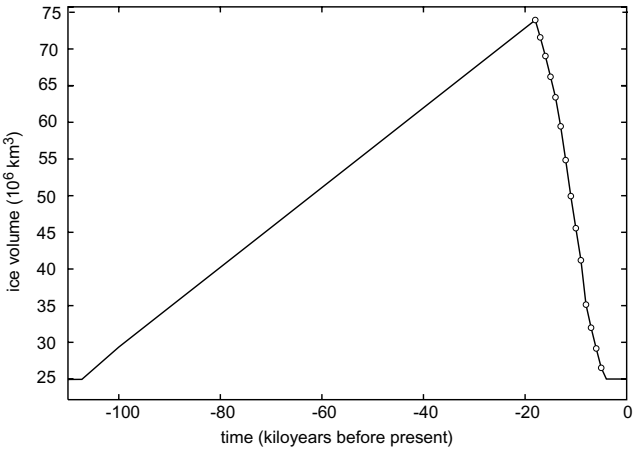

Figure 1. The ice history used to load the Earth, shown as the total ice volume in millions of cubic kilometres versus time in kiloyears (before present). The open circles show the data provided by the ICE-3G deglaciation model. To this we include a 90 kyr linear glaciation period, and linearly interpolated ice height between the ICE-3G data.

where σ_{app} is the applied pressure from the loads, r_s is the Earth radius and n_i is the surface normal. The applied pressure at the surface can be written as

$$\sigma_{app}(\theta, \varphi, t) = \rho_w L_i(\theta, \varphi, t) + \rho_w L_o(\theta, \varphi, t), \tag{6}$$

where L_i is the height of the ice and L_o is the height of the ocean water relative to their initial values at the onset of glaciation. Both the ice and ocean are given the density of water, ρ_w. The ice load is based on the ICE-3G deglaciation model (Tushingham & Peltier 1991), which specifies ice height globally at 14 time epochs separated by 1 kyr intervals. The complete time dependence is made piecewise-linear by linearly interpolating the ice height between specified epochs, and providing a 90 kyr linear ramp up to glacial maximum. The ice-covered area is kept fixed during the 90 kyr ramp. The resulting total ice volume is shown in Fig. 1. The ocean load is determined by the sea level equation, discussed in Section 2.2.2

The boundary conditions for eq. (3) are

$$\phi(r^+) = \phi(r^-) \qquad \text{for } r = r_s \text{ and } r = r_b,$$

$$n_i \phi_{,i}(r^+) + 4\pi G \rho(r^+) n_i u_i(r) = n_i \phi_{,i}(r^-) + 4\pi G \rho(r^-) n_i u_i(r) \qquad \text{for } r = r_s \text{ and } r = r_b,$$

where $\rho(r^+) = 0$ at the outer surface.

Treating the mantle as a viscoelastic (Maxwell) incompressible solid governed by the equations above, the stress tensor σ_{ij} and strain tensor ϵ_{ij} are related by

$$\sigma_{ij} + \frac{\eta}{\mu}\dot{\sigma}_{ij} = -\left(P + \frac{\eta}{\mu}\dot{P}\right)\delta_{ij} + 2\eta\dot{\epsilon}_{ij}, \tag{7}$$

where η is the viscosity, μ is the shear modulus, P is the pressure, δ_{ij} is the Kronecker delta and the dot indicates a time derivative. Both the surface and CMB are allowed to deform freely as the surface is subjected to the time-dependent load.

Unless otherwise noted, density, shear modulus and gravitational acceleration are constant throughout the mantle. Their values, along with other parameters used throughout this study, are shown in Table 1.

Table 1. Model parameters.

Parameter	Value
Radius of Earth, r_s	6.3700×10^6 m
Radius of CMB, r_b	3.5035×10^6 m
Mantle shear modulus, μ	1.4305×10^{11} Pa
Mantle density, ρ_o	4400 kg m^{-3}
Density change across CMB, $\Delta\rho$	5425 kg m^{-3}
Gravitational acceleration, g	9.8 m s^{-2}

2.2 Solution methods with degree-one deformation, polar wander and ocean load

For purposes of benchmarking and comparison, the forward problem is solved with two distinct methods: a spherical finite-element code that can accommodate 3-D viscosity variations and a semi-analytical spectral method that can solve for PGR deformation on spherically symmetric earth models. We use the finite-element code CitcomSVE to solve the viscoelastic problem in spherical geometry. It was derived from a code developed for viscous mantle convection (Zhong *et al.* 2000) by discretizing the time-dependent rheology, allowing viscous and elastic displacement and strain to be treated incrementally, and accommodating self-gravitation. The implementation of the viscoelastic solution in the finite-element code is discussed in detail in Zhong *et al.* (2003). The spectral method, similar to that of Wu & Peltier (1982) and Wahr *et al.* (2001), solves the equations in the Laplace transform domain using the collocation technique (Mitrovica & Peltier 1992). It computes the Love numbers $h_l(t)$ and $k_l(t)$ for surface vertical displacement and potential, respectively, for each spherical harmonic degree l.

To make the PGR model more realistic, both computational methods were augmented to include the effects of centre of mass motion, gravitationally responsive ocean loading and feedback between deformation and the shifting rotation axis of the Earth. This study is the first to our knowledge to implement these combined effects in a 3-D numerical model, although they have been previously considered independently (Wu & van der Wal 2003) and have been incorporated in spectral methods (Han & Wahr 1989; Mitrovica *et al.* 2005). We discuss the implementation of each of these effects, first with some general comments and then the method-specific details.

2.2.1 Centre of mass motion

Motion of the centre of mass of the Earth, which can be described with spherical harmonic degree one, is often neglected since it may be accommodated by a simple shift in the origin of the coordinate system. However, if any processes obtain that couple responses at different spherical harmonic degrees, explicit calculation of the degree-one response is required. For example, the degree-one response must be considered when implementing the sea level equation due to the degree-one power in the shape of the oceans. Lateral variations in viscosity or lithospheric thickness will also couple responses at different harmonics.

In both computational methods, our goal is to measure the degree-one deformation with respect to an origin at the centre of mass of the Earth-plus-load system. In this coordinate system, the reference frame used for satellite observations, the degree-one component of the potential outside the Earth is identically zero. Here and below, 'CM' refers to the centre of mass of the Earth–load system.

Finite-element method. CitcomSVE provides a coordinate system that is fixed at the centre of the initial, spherical Earth (we shall call this coordinate system the 'FE frame'). The task is to ensure that the recorded results are those that would be observed in the CM coordinate system, whose origin is defined by the centre of mass of the Earth–load system. This is accomplished by mimicking the loading as viewed from the CM frame, performing the calculation of the deformation normally in the FE frame, and then reporting the results with respect to the CM frame.

As mentioned above, the finite-element code implements the time dependence incrementally, in a series of 'time steps' (each spanning 25 yr during deglaciation and relaxation). At the beginning of each time step a new incremental load is applied to the Earth's surface and CMB, consisting of (1) the incremental deformation of the surface and CMB from the previous time step and (2) changes in ice and ocean loads (details of this procedure can be found in Zhong *et al.* (2003)). If the centre of mass of this incremental load (with respect to the FE frame) is $\mathbf{r}_{cm}$, then in the CM frame application of this load would be accompanied by a simultaneous translation of the rest of the Earth of $-\mathbf{r}_{cm}$. Thus in order to mimic the state of the loading as seen from the CM frame, we add an additional surface mass of $-r_{cm}\Delta\rho\cos\vartheta$ at the CMB, and $-r_{cm}\rho_o\cos\vartheta$ at the outer surface, where ϑ is the angular distance from the direction defined by $\mathbf{r}_{cm}$ (other symbols from Table 1). These additional loads correspond to the translation of the sphere of $-\mathbf{r}_{cm}$. The calculation of the Earth's deformation in the FE frame then proceeds normally for this time step, with loads which are identical to those that would be experienced in the CM frame. The computed results only differ from those in the CM frame by the fact that the latter is displaced by $\mathbf{r}_{cm}$ from the FE coordinate system. Thus, at the end of the time step, $\mathbf{r}_{cm}$ is subtracted from the incremental deformation before recording it. The net effect is equivalent to what would be observed in the the CM coordinate system.

It may also be noted here that some formulations of the degree-one calculation are vulnerable to non-unique solution, since translation of the entire Earth–load system may occur freely. However, this issue does not plague the above implementation. This is because as long as the loading is identical to that viewed from the CM frame, the degree-one gravitation outside the Earth is cancelled exactly, so there is no force available to initiate a net translation of the Earth.

Spectral method. Calculation of the Love numbers occurs in a coordinate system whose origin is already, by design, at the centre of mass of the Earth–load system. However, naïvely applying the standard propagation-matrix methods to the degree-one Love numbers results in the attempt to invert a singular matrix. This occurs because of a problem unique to the solution at degree one: translation of the entire Earth is a solution of the homogeneous (zero external force) differential equations. We correct for this problem by removing that part of the degree-one solution that corresponds to whole Earth translation (Farrell 1972); the remaining solution provides the degree-one deformation in the CM reference frame.

2.2.2 Sea level equation

In addition to the glacial mass, significant surface loading is provided by the ocean in two forms: increased volume from melted ice and the response of the fluid ocean to topography and geoid changes. These effects are included via the sea level equation, which gives the change in height of the ocean load, L_o, since the onset of glaciation (Farrell & Clark 1976):

$$L_o(\theta,\varphi,t) = [N(\theta,\varphi,t) - U(\theta,\varphi,t) + c(t)]\, O(\theta,\varphi,t), \qquad (8)$$

where N and U are the PGR-induced perturbations to the geoid and surface displacement, $O(\theta, \varphi)$ is the ocean function (1 over the ocean, 0 elsewhere). c is the eustatic sea level, given by

$$c(t) = \frac{1}{A_o(t)} \left(-\frac{M_{ice}(t)}{\rho_w} - \int (N - U)\, O\, d\Omega \right), \tag{9}$$

where A_o is the area of the oceans, M_{ice} is the mass of the ice sheets, ρ_w is water density and $d\Omega$ is an element of solid angle.

The time dependence of the ocean function comes from shoreline migration caused by (1) on-lap and off-lap in regions of local sea level change and (2) ocean influx in regions of retreating marine-based glaciers (Mitrovica 2003). Kendall *et al.* (2005) have shown that in the vicinity of glaciated regions, such as Hudson Bay and along the east coast of North America, contribution (2) has a much more significant impact on sea levels than does (1). They have also shown that the effect of (1) remains localized to very near shorelines. Since in this study we only consider local measures of PGR near Hudson Bay, and global measures of PGR of much longer wavelength than those affected by factor (1) (estimated to be at spherical harmonic degree 80 and above), we neglect the effect of on- and off-lap due to local sea level change. However the time dependence of the ocean function due to water influx, effect (2), is implemented—as described presently.

In regions where retreat of the edge of the ice sheet is accompanied by an advance of the ocean, the value of the ocean function must change from 0 to 1. While at each ICE-3G epoch (the circles in Fig. 1), the ocean function is well defined everywhere to be 1 or 0, at times between these epochs it is allowed to vary smoothly from 0 up to 1 where the ice is disappearing along the edge. This treatment prevents the sudden ocean inundation of deglaciated regions every 1000 yr, it approximates the smooth retreat of the edge of the ice sheet and it avoids the unrealistic effects of a negative near-field ocean load discussed in Milne *et al.* (1999). This implementation of the ocean function is easily incorporated into the finite-element and spectral methods, as described below.

Finite-element method. Implementation of the sea level equation is straightforward in the finite-element code. At each time step, the ocean load L_o is calculated with eqs (8) and (9) using the current (linearly interpolated) values of ice height and ocean function. Since N and U depend on the ocean load, in principle an iterative approach should be used between N, U and L_o. For the first few time steps, full iteration is performed until these fields cease to change under further iteration (typically four or five iterations are required). However, full iteration is only performed for the first few time steps; for subsequent time steps we use values of N and U extrapolated from the previous two time steps. This significantly improves the computational efficiency. The error introduced with this approximation can be measured by repeating the calculations with full iteration at every time step, and is found to be negligible.

Spectral method. Since there is no 'time stepping' in the spectral calculation (time dependence is implicit in the Laplace transform domain), the spherical harmonic spectrum of a loading history that is piecewise linear in time need only be specified by giving the spectrum at a few designated times (14 1-kyr time intervals, in the case of ICE-3G)—the linear ramp between these times can be transformed exactly into the Laplace transform domain. Thus calculation of the ocean load, eq. (8), need only be performed at these few designated times. The intermediate values of the ocean function (between 0 and 1) approximate the effect of water influx at a retreating ice sheet.

Calculation of the ocean load is performed iteratively, beginning by setting $U = N = 0$ in eq. (8) for an initial ocean load at each epoch. The resulting values for topography and geoid are then used in another calculation of L_o, and the forward problem is solved again with the new load. Iteration continues until there is no appreciable change in the topography and geoid (we find that this criterion rarely requires more than two iterations).

Compared with all other calculations performed by the spectral method, including solution for the Love numbers themselves, the sea level equation is much more computationally expensive. The primary reason is the fact that the Earth's response must be calculated in the (spherical harmonic) spectral domain, while eq. (8) must be performed in the spatial domain. This requires the transformation of $N_{l,m} - U_{l,m}$ to $N(\theta, \varphi) - U(\theta, \varphi)$, for multiplication with $O(\theta, \varphi)$ at each 'time node' of the piecewise-linear loading, and then the transformation of the resulting $L_o(\theta, \varphi, t)$ back to the spectral domain for use as a new load in the next iteration.

2.2.3 Polar wander

Changes in surface topography, CMB topography and ice and ocean loading will perturb the Earth's inertia tensor and consequently the Earth's rotation vector. Changes in Earth rotation, in turn, feed back to deformation via perturbation of the centrifugal potential. To describe this effect, we write the Earth's angular velocity as $\boldsymbol{\omega} = \Omega(m_x, m_y, 1 + m_z)$, where Ω is its unperturbed magnitude and the m_i are the dimensionless Cartesian components of the perturbation. It will be convenient to use the complex quantities $m_\pm = m_x \pm i m_y$. Similarly, for perturbations to the Earth's inertia tensor (due to deformation and loads), we use $I_\pm = I_{xz} \pm i I_{yz}$. For periods much longer than the Chandler wobble, Lambeck (1980) shows that

$$m_\pm = \frac{I_\pm}{C - A}, \tag{10}$$

where C and A are the unperturbed principal polar and equatorial moments of inertia. We may neglect changes in m_z, which are much smaller than changes in m_x or m_y.

Our analysis differs from previous work (for example, Wu & Peltier 1984; Han & Wahr 1989; Bills & James 1997) by including the influence of the small non-hydrostatic component of the Earth's ellipticity, which serves to stabilize the rotation axis and damp its response to PGR-induced deformation. Without this contribution, polar motion can be highly unstable since there is no 'preferred' direction for the rotation axis. The influence of this contribution and a method for including it are discussed in detail by Mitrovica *et al.* (2005). Briefly, the denominator in eq. (10) should include a hydrostatic component and a much smaller non-hydrostatic component: $C - A = (C - A)_{hyd} + (C - A)_{nonhyd}$. We express this as

$$m_\pm = \frac{I_\pm}{(C - A)_{hyd}(1 + \delta)}, \tag{11}$$

where δ is estimated to be about 0.8 per cent and $(C - A)_{hyd}$ describes purely hydrostatic oblateness in response to rotation. In particular, $(C - A)_{hyd}$ is derived from the infinite-time response of the Earth to tidal forcing at spherical harmonic degree two, using the same Earth model to be used throughout the calculation (Table 1). Here, the infinite-time limit includes complete relaxation of a highly viscous lithosphere—such a lithosphere behaves elastically on timescales characteristic of glacial isostatic adjustment. Such an excess ellipticity is observed in the real Earth (e.g. Munk & MacDonald 1960), due perhaps to plate tectonics, mantle convection or a fossil rotational bulge, and its source is long-lived compared

with the timescales of glacial isostatic adjustment. Thus, once it is determined, the value $(C - A)_{\rm hyd}\,(1 + \delta)$ remains constant throughout the calculation.

That such a correction to $(C - A)_{\rm hyd}$ provides rotational stability can be demonstrated as follows. Suppose that before the onset of glaciation, the Earth's principal moments of inertia, C and A, were due solely to rotational hydrostatic equilibrium. Then upon formation of a glacier not exactly on the rotational pole, the rotation axis would begin to shift away from the extra mass, 'pushing' it outwards towards the rotational equator. Even if the glacier were to then rapidly ablate, the momentary application of a new centrifugal potential (due to the new location of the pole) would cause the Earth's rotational bulge to partially relax into a new hydrostatic equilibrium, such that when all surface mass perturbations are gone there would remain a net *permanent* shift in the location of the rotational axis. Suppose, on the other hand, that the initial ellipticity of the Earth was slightly in excess of pure hydrostatic equilibrium, as described by $(C - A)_{\rm hyd}\,(1 + \delta)$; there would then exist a preferred direction of the rotation axis. In this case, after a transient perturbation to the Earth's inertia tensor—after the load and any resulting deformation had completely disappeared—the rotational axis would ultimately relax back to its original configuration, guided by the more permanent non-hydrostatic feature. Much greater detail on this effect can be found in Mitrovica *et al.* (2005).

An important property of the effect of polar wander is that it only acts directly on the geoid with a $Y_2^{\pm 1}$ spherical harmonic angular dependence. Asymmetries, such as laterally varying viscosity or the sea level equation, may then couple responses at other degrees. That the direct influence of a small polar shift $m_\pm$ is restricted to degree two, order ± 1, is due to the fact that it induces a change in centrifugal potential given by

$$\Delta\phi_{\rm c} = \sqrt{\frac{2\pi}{15}}\,\Omega^2 r_{\rm s}^2\left(m_- Y_2^1 - m_+ Y_2^{-1}\right), \tag{12}$$

where $r_{\rm s}$ is the Earth's mean radius (Lambeck 1980). $\Delta\phi_{\rm c}$, having a $Y_2^{\pm 1}$ spherical harmonic angular dependence, will induce deformation (and therefore geoid change) only at degree two, order ± 1.

The response of the Earth's rotation to changes in surface mass and topography feeds back upon surface deformation: the mass changes alter the Earth's inertia tensor, which shifts the rotational axis (eq. 11), which changes the centrifugal potential (eq. 12), which in turn forces and deforms the Earth. This feedback may be modelled by an iterative method, as we do in the finite-element implementation, or may be solved in a closed form, as we do in the spectral method (Han & Wahr 1989).

Finite-element method. In the spatial domain of the finite-element method, the implementation is straightforward: every time the code calculates the potential, an extra step is performed that adds in the perturbed centrifugal potential. The only required change to the code is this addition to the self-gravitational potential of a centrifugal potential at degree two, order ± 1, which then feeds back upon deformation only by the normal reaction of the solid Earth to gravitational forcing. Calculation of this extra contribution to the potential proceeds as follows.

At the beginning of each time step, the change to the inertia tensor, $I_\pm$, is calculated from changes in boundary deformation and surface ice and ocean loads. With $I_\pm$, eq. (11) is used to obtain the new rotation axis in the form of $m_\pm$. From this, the first-order change in centrifugal potential is given by eq. (12), which is added to the gravitational potential. As with the sea level equation, the potential calculation is performed iteratively for the first few time steps: the incremental potential forces the Earth, and the resulting deformation gives a slightly different gravitational potential, so the new potential is used to force the Earth. The iteration for this time step ceases when deformation converges. Subsequent time steps use an extrapolated estimate of the potential, including the centrifugal contribution. As before, the error of this approximation is negligible, as determined by comparison with cases in which full iteration occurs at every time step.

Spectral method. In the Laplace transform domain, the interdependent relation between deformation and centrifugal potential may be solved in a closed form and expressed as a single Love number that includes the polar wander feedback (Han & Wahr 1989; Mitrovica *et al.* 2005). Since the rotational effects only appear at spherical harmonic degree two, order ± 1, we calculate special forms for the $h_2^{\pm 1}$ and $k_2^{\pm 1}$ Love numbers, which give the vertical displacement and surface potential, respectively. In the Laplace transform domain, these are

$$k_2^{\pm 1} = k_2^{\rm L} + k_2^{\rm T}\left(\frac{1 + k_2^{\rm L}}{k_{\rm f} - k_2^{\rm T}}\right), \tag{13}$$

$$h_2^{\pm 1} = h_2^{\rm L} + h_2^{\rm T}\left(\frac{1 + k_2^{\rm L}}{k_{\rm f} - k_2^{\rm T}}\right), \tag{14}$$

where the superscripts L and T designate the load and tide Love numbers, respectively. The quantity $k_{\rm f}$ is called the fluid Love number, as it represents the fluid limit (i.e. $s \to 0$ or $t \to \infty$) of $k_2^{\rm T}$.

We modify the value $k_{\rm f}$ in a way physically equivalent to eq. 11, as discussed in Mitrovica *et al.* (2005), letting

$$k_{\rm f} = (1 + \delta)k_2^{\rm T}(s = 0), \tag{15}$$

where $\delta = 0.008$, as before. The $s \to 0$ limit of $k_2^{\rm T}$ should include relaxation of all stresses in the lithosphere. To ensure this, the earth model uses a lithosphere of very high viscosity, 10^{25} Pa s, which behaves elastically in the timescales of glacial isostatic adjustment, but holds no stress in the $s \to 0$ limit.

The modification expressed in eq. (15) avoids the instability in the rotational feedback (which can be seen in the form of a zero denominator in eqs (13) and (14) in the limit $s \to 0$), while accounting for the effect of non-hydrostatic contributions to the Earth's ellipticity. With the modification in eq. (15), the Love numbers given in eqs (13) and (14) may be used to calculate the $l = 2$, $m = \pm 1$ response, corrected for polar wander.

2.3 Derivation of a 3-D viscosity model

A 3-D mantle viscosity model is needed to examine the effects of laterally varying viscosity on PGR. Here we describe the derivation of the viscosity model, using seismic structure, thermodynamics and rheological equations. Greater detail is given in Appendix A.

We begin with a composite of two different shear wave mantle models: the long-wavelength global model S20RTS (Ritsema *et al.* 1999) and the higher-resolution model NA00 of van der Lee (2002) beneath North America. The reason for using a special model for North America is that much of our work centres on Laurentia. The shear velocities are converted to a 3-D temperature structure. For depths less than 400 km this is accomplished by a direct conversion based on mineral properties (Shapiro & Ritzwoller 2004). At greater depths, a constant conversion to density variation is used ($\delta \ln \rho / \delta \ln V_s = 0.3$, Karato 1993). The density variation may then

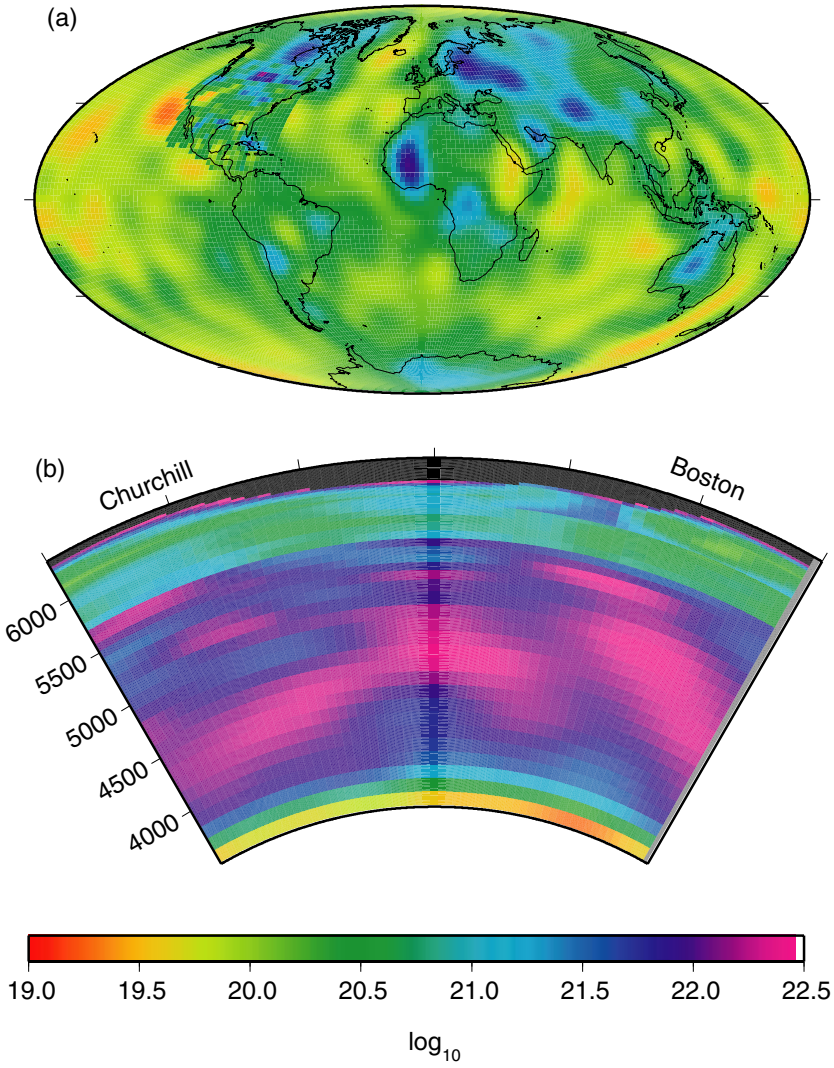

Figure 2. Two views of the 3-D viscosity model: (a) at a depth of 230 km, (b) a slice under Churchill (on the western shore of Hudson Bay) and Boston.

be multiplied by a depth-dependent thermal expansivity to obtain 3-D temperature variations $\delta T(\mathbf{r})$. The latter is added to the adiabatic temperature gradient to obtain a global 3-D temperature field, $T(\mathbf{r})$. The 3-D viscosity $\eta(\mathbf{r})$ is then computed with

$$\eta(\mathbf{r}) = A_0 \exp\left(\gamma \frac{T_{\rm m}(r)}{T(\mathbf{r})}\right), \tag{16}$$

where $T_{\rm m}(r)$ is the melting temperature, γ is an activation parameter and A_0 is a coefficient. We may choose γ and the leading constant A_0 separately for the upper and lower mantle to obtain a desired viscosity discontinuity at 670 km depth (for example, a jump by a factor of 30, or a factor of 2).

The resulting 3-D viscosity model is shown in Fig. 2(a) at a depth of 230 km, and in Fig. 2(b) as a cross-section under Hudson Bay and Boston. For this particular model, we have chosen a value of $A_0 = 2 \times 10^9$ Pa s in the upper mantle and $A_0 = 1.2 \times 10^{13}$ Pa s in the lower mantle, giving a viscosity discontinuity of 30× at a depth of 670 km. Lateral variations of about one order of magnitude are typical, with minimum and maximum viscosities at a given depth typically two to three orders of magnitude apart (grey region of Fig. 3). The higher resolution used around North America is also visible in Fig. 2(a).

For another view of the 3-D structure, 1-D (spherically symmetric) models are formed from weighted averages of the lateral viscosity variations of the 3-D model. All viscosity averages are actually averages of the logarithm of the viscosity. The averaging includes an arbitrary weighting function, $w(\theta, \varphi)$, and treats the elastic lithosphere specially—it is described fully in Appendix B. These 1-D derivatives of the 3-D model show the local structure in sites of interest, as well as globally averaged structure; they will also be used later in Section 3.4.

Fig. 3 shows four such 1-D models: a 'global' average ($w = 1$ everywhere), an 'ice-weighted' average (w proportional to the height of the ice at the last glacial maximum), a 'Hudson Bay' average ($w = 1$ around Hudson Bay, within 100 km of the coastline, and $w = 0$ elsewhere), and an 'east coast' average ($w = 1$ along the east coast of North America between Newfoundland and Virginia, within 100 km of the coastline, and $w = 0$ elsewhere). The ice-weighted model takes its viscosity primarily from Laurentia, Scandinavia and Antarctica. It and the Hudson Bay average both reflect mostly continental structure, with a thicker lithosphere and higher upper mantle viscosity. The east coast average, taken from the continental margin, has a thinner lithosphere. Also shown in Fig. 3 by the grey region is the full range of the lateral variations of the 3-D model.

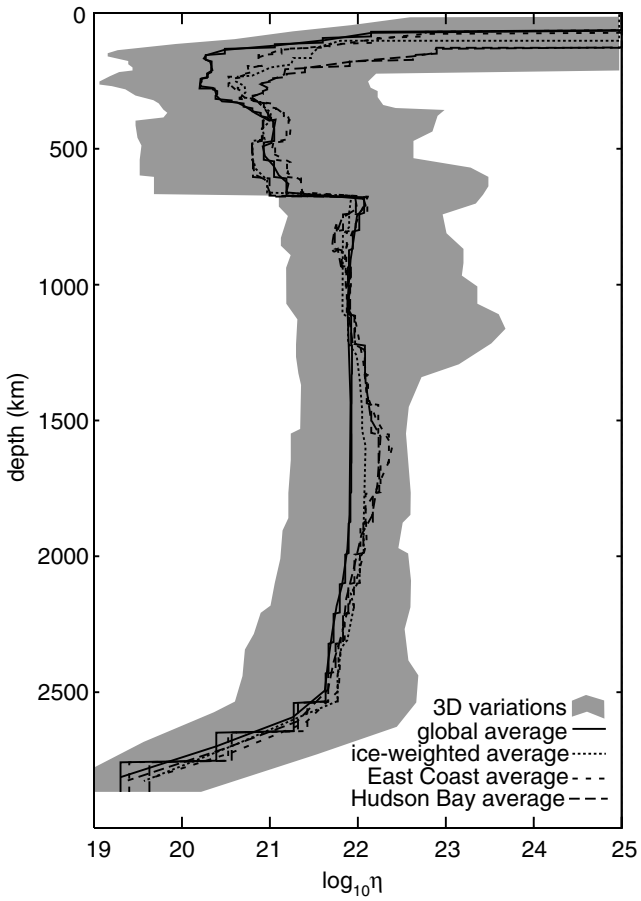

Figure 3. Four 1-D averages of the 3-D viscosity model, defined by different weighting functions w: a 'global' average ($w = 1$ everywhere), an 'ice-weighted' average (w proportional to the glacier height at the last glacial maximum), a 'Hudson Bay' average ($w = 1$ around Hudson Bay, within 100 km of the coastline and $w = 0$ elsewhere), and an 'east coast' average ($w = 1$ along the east coast of North America between Newfoundland and Virginia, within 100 km of the coastline and $w = 0$ elsewhere). The grey region shows the extent of the full lateral variations of the 3-D model.

3 RESULTS

3.1 Benchmarks

When the earth model used to calculate viscoelastic response is 1-D (spherically symmetric), the results of the finite-element and spectral methods may be benchmarked against each other. In this section we present how the two methods compare globally in topography and geoid solutions.

For the benchmarks, we use an earth model with the properties shown in Table 1. The mantle viscosity is set to 2×10^{21} Pa s below 670 km depth, and 10^{21} Pa s in the upper mantle. The lithosphere is given a thickness of 120 km. Surface loading is provided by the modified ICE-3G model discussed in Section 2.1, and includes the ocean load only in the cases that implement the sea level equation.

For all finite-element calculations in this study (with the exception only of the resolution convergence tests, mentioned below), we use the highest resolution available to us computationally. This highest resolution has 76 800 elements laterally (across the entire sphere), and 48 elements vertically (between the surface and the core–mantle boundary). The average element spans about 80 km laterally and 20–110 km vertically, with the finest resolution in the upper mantle. The time steps are 200 yr in length during the ramp up to glacial maximum, and 25 yr in length thereafter (see Fig. 1), with a total of 1170 time steps. The finite-element calculation of the potential is performed up to spherical harmonic degree and order 32.

Table 2. Benchmark comparisons between finite-element and spectral methods.

Field	Time	D1	SLE	PW	SLEPW
Topo.	−28 kyr	0.758	1.140	0.893	1.149
	−10 kyr	0.882	1.371	1.135	1.378
	Present	1.796	4.129	3.336	3.841
Topo. rate	−28 kyr	0.732	1.230	1.007	1.240
	−10 kyr	0.634	0.870	0.606	0.895
	Present	1.727	2.044	1.581	2.059
Geoid	−28 kyr	0.990	0.993	0.248	0.903
	−10 kyr	0.738	1.162	1.034	1.589
	Present	0.812	1.623	0.954	1.257
Geoid rate	−28 kyr	1.960	2.045	0.321	0.824
	−10 kyr	1.060	1.082	0.479	0.837
	Present	0.816	1.007	0.805	1.231

The fields we compare are topography, rate of change of topography, geoid and rate of change of geoid, and are measured at three times: −28 kyr (near the end of the ramp up to glacial maximum), −10 kyr (during deglaciation) and the present (Fig. 1). We express the field of interest at a given time t_0 by $f_{\mathrm{FE}}(\theta, \varphi, t_0)$ and $f_{\mathrm{S}}(\theta, \varphi, t_0)$ for the finite-element and spectral methods, respectively. The difference in the two fields is then measured by

$$\varepsilon = \sqrt{\frac{\int (f_{\mathrm{FE}} - f_{\mathrm{S}})^2 \, dA}{\int f_{\mathrm{S}}^2 \, dA}}, \tag{17}$$

where the integral is over the entire Earth's surface. Table 2 shows the dimensionless percentage difference for four cases implementing the various effects described in Section 2.2. All cases implement the degree-one response (centre of mass motion) described in Section 2.2.1

Case 'D1' is only different from the previously published benchmark by Zhong *et al.* (2003) in its implementation of the degree-one response (no ocean load nor polar wander). For this case the agreement between the finite-element and spectral methods is generally very good, always below 2 per cent. Case 'SLE' includes effects of the ocean load via the sea level equation; it does not include the polar wander effect but it does include the degree-one response (which is necessary due to the degree-one power in the ocean load). Here, except for a 4 per cent difference in present-day global topography, the agreement for all fields and times is about 1–2 per cent. Case 'PW' includes the effects of polar wander; it includes no ocean load but does include the degree-one effect, whose independent benchmark demonstrated very close agreement. Agreement for this case is nearly the same as for case 'D1' in all fields except present-day topography (3.3 per cent). Case 'SLEPW' includes the sea level equation, polar wander and, as in all cases, the degree-one effect. Agreement here closely follows results for case 'SLE'. Our implementation of the sea level equation appears to introduce slightly more error than does that of polar wander. In all cases, the most sensitive field and time is present-day global topography. This is partially due to the smaller magnitude of present-day topography after completion of much of the isostatic adjustment (thus a smaller denominator in eq. 17). The geoid fields tend to agree better because

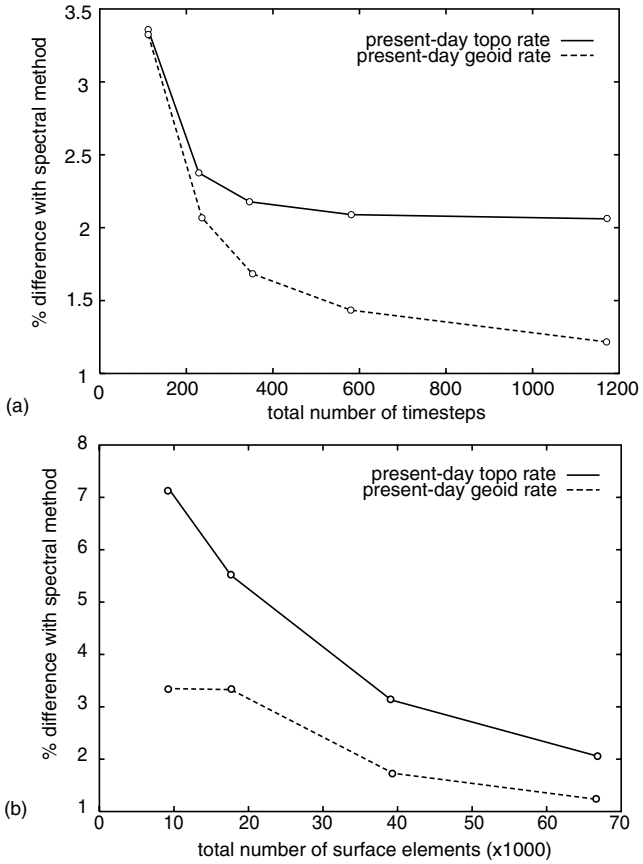

Figure 4. Convergence of finite element results to spectral results with increased resolution in the finite element code (a) temporally and (b) spatially. The figures show the percent misfit of two fields: the rate of change of present-day global topography (solid line) and the rate of change of present-day geoid (dashed line). On the abscissa is the total number of time steps (a) and total number of global surface elements (b) used in the finite element calculation. The case compared is 'SLEPW', including all effects described in Section 2.2. The remaining misfit in the highest resolution case (corresponding those in Table 2) appear to be primarily limited by spatial resolution.

the finite-element code can reproduce the long-wavelength signals well.

Fig. 4 demonstrates the convergence of the finite element results to those of the spectral method for the case 'SLEPW' for the rate of change of present-day global topography and the rate of change of present-day geoid. Fig. 4(a) shows the improved agreement as the time resolution is increased from a total number of 117 time steps (250 yr step during deglaciation) to 1170 time steps (25 yr step). It is apparent that significant improvement cannot be gained by increasing the time resolution. Fig. 4(b) shows the convergence of the finite-element result to the spectral result as the lateral spatial resolution is increased from 19 200 surface elements (about 160 km span) to 76 800 surface elements (80 km), the maximum available to us. Although agreement with the spectral solution, already reduced to a few per cent, may apparently be further improved with greater spatial resolution, the computational demands on memory make this currently unavailable to us. Note that the highest resolution results in Fig. 4 correspond to those values given in Table 2.

The agreement between the spectral and finite-element methods may be compared visually for a few of the long-wavelength components of the global relative sea level (RSL). We define RSL as simply topography minus geoid, where both topography and geoid

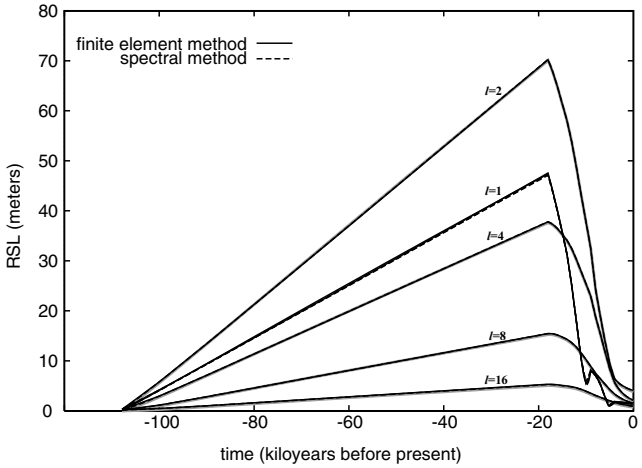

Figure 5. Relative sea level (RSL) at spherical harmonic degrees 1, 2, 4, 8 and 16. Finite-element results use the solid line; the spectral method uses the dashed line (which may not be visible due to overlap with the solid line).

are measured relative to their pre-glaciation values. Fig. 5 shows the time dependence of RSL at spherical harmonic degrees 1, 2, 4, 8 and 16. The case shown is 'SLEPW', which includes the sea level equation and polar wander effects. The value shown for spherical harmonic degree l, called $g_l(t)$ here, is a composite measure of all spherical harmonic orders (m) for that degree, given by

$$g_l(t) = \sqrt{\frac{1}{l+1}\sum_{m=0}^{l}\left|\tilde{g}_{l,m}(t)\right|^2}, \tag{18}$$

where the $\tilde{g}_{l,m}(t)$ represent the complex spherical harmonic coefficients of the RSL response. For these long-wavelength signals, the comparison between the finite-element and spectral method solutions (the solid and dashed lines, respectively) shows no discernible difference. The small differences expressed in Table 2 are too small to be seen here.

Fig. 6(a) shows RSL at spherical harmonic degree two, order 1, where the polar wander feedback is acting directly. The cases shown are 'SLEPW' (labelled 'including polar wander') and 'SLE' (labelled 'no polar wander'). Again, the finite-element (solid lines) and spectral method (dashed lines) agree very well.

3.2 Effects of degree-one deformation, sea level equation and polar wander

To demonstrate the contributions of the processes described in Section 2.2, we present some visual comparisons of changes in relative sea level (RSL) upon introduction of each effect.

Fig. 5 shows the time dependence of RSL at spherical harmonic degrees 1, 2, 4, 8 and 16 for case 'SLEPW' (including the sea level equation and polar wander effects). The response at degree one is roughly equal in magnitude to the response at the other long wavelengths, demonstrating its important contribution to the total RSL signal.

Fig. 6(a) shows the influence of the polar wander feedback on RSL at spherical harmonic degree two, order 1. Including the polar wander feedback tends to reduce the topography response (Han & Wahr 1989). As shown, the RSL history for case 'SLEPW' is about half that of case 'SLE', which is identical except for the absence of this effect. Fig. 6(b) shows the rate of true polar wander over the past 100 kyr for the same two cases. Whether or not the polar

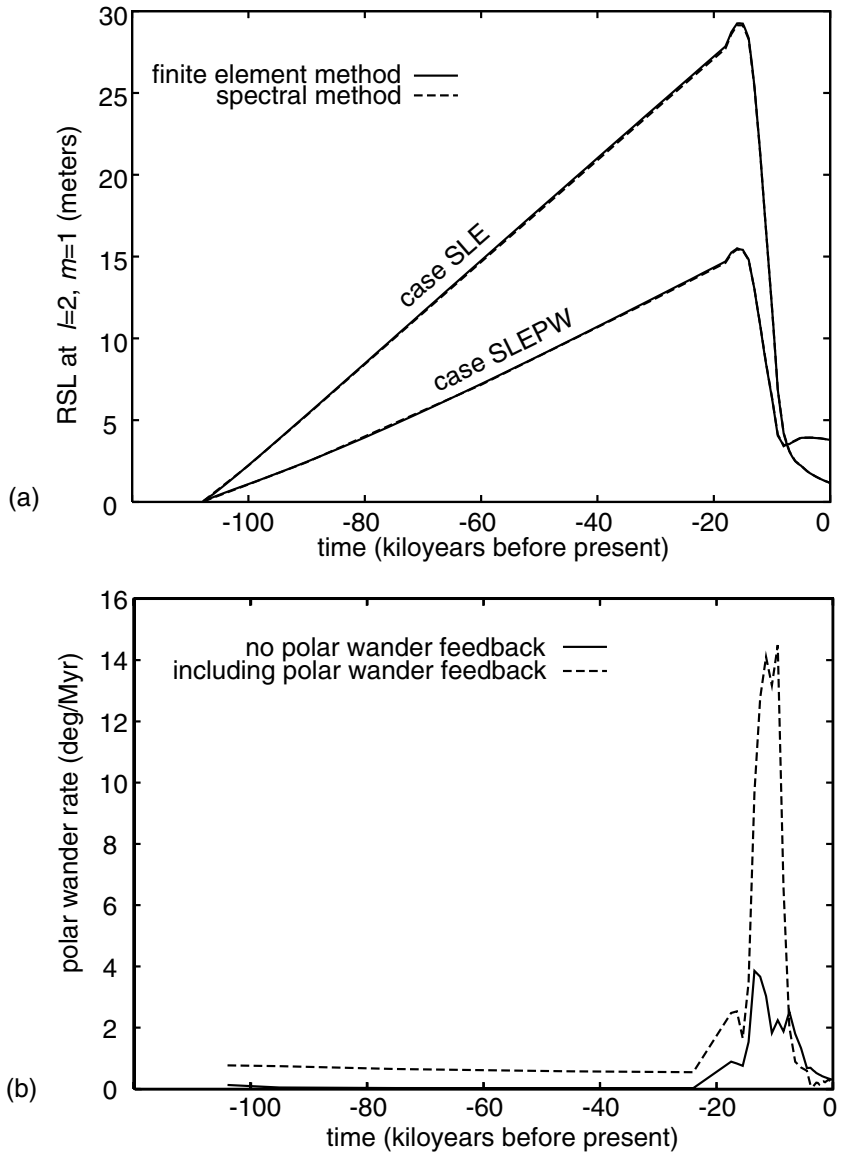

Figure 6. (a) RSL at spherical harmonic degree two, order 1, with and without the polar wander feedback. (b) Motion of the pole since the onset of glaciation. The two cases shown are 'SLEPW' (includes polar wander) and 'SLE' (without polar wander feedback). In (a) agreement between the two methods may be seen in the overlapping solid line (finite element) and dashed line (spectral method).

wander feedback is included, the position of the rotational axis can be computed from eq. (11) and from MacCullagh's formula, which relates the inertia tensor to the $l = 2$ components of the Earth's gravitational potential (Lambeck 1980, eq. 2.4.5). As the figure shows, including the polar wander feedback greatly increases the motion of the rotational axis.

As discussed earlier (eq. 12), the polar wander feedback acts directly only on the degree two, order ± 1 potential. However, certain model asymmetries can couple responses at spherical harmonics of different degrees; in these cases introduction of the polar wander effect will also indirectly affect the potential and topography at other angular degrees. In this paper we consider two such asymmetries: lateral variation of mantle viscosity, and the sea level equation. To demonstrate this coupling, Fig. 7 shows the per cent change in present-day surface potential at spherical harmonic degrees up to 20 upon introduction of the polar wander effect for each of the coupling cases: 3-D viscosity variations (using the model shown in Fig. 2) and the sea level equation. The value shown, a composite measure of all spherical harmonic orders (m) for each degree (l) given by eq. (18), compares a case that implements the polar wander feedback with an otherwise identical case without it. Degree two order 1 is omitted in the composite value for $l = 2$; the difference at this harmonic is about 80 per cent. The black bars compare spherical harmonic components of surface potential for the 3-D earth model (shown in Fig. 2) with no sea level equation, to isolate the coupling effects of lateral viscosity variations. The grey bars compare two 1-D viscosity models that implement the sea level equation, cases 'SLE' and 'SLEPW'. We see that lateral viscosity variations (black bars) couple different harmonics to the $l = 2$, $m = 1$ harmonic much more strongly than the sea level equation does (grey bars). Still, those other harmonics change by only a fraction of 1 per cent. Note that this small value of 1 per cent is only a measure of how the $l = 2$, $m = 1$ potential couples to the potential at other harmonics; the total influence of lateral viscosity variations or the sea level equation is

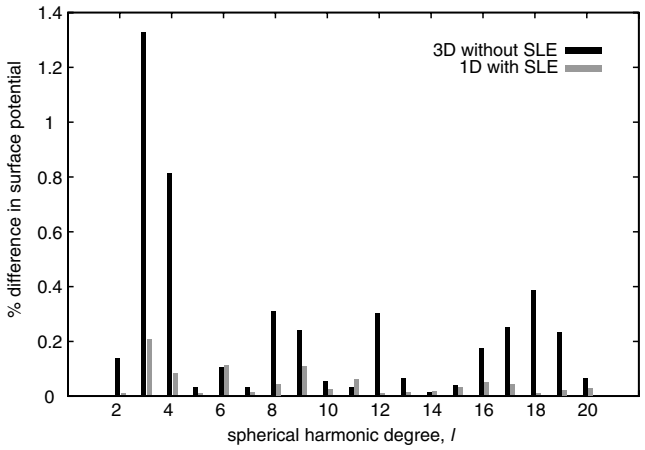

Figure 7. Coupling of polar wander effects to other spherical harmonic degrees due to lateral viscosity variations (black) and the sea level equation (grey). Shown is the per cent difference in surface potential at all spherical harmonic degrees between cases with the polar wander feedback included versus not included (the directly affected $l = 2$, $m = 1$ component, about 80 per cent, is removed from the degree-two bars).

a combined effect of intercoupling between all harmonics, and is much more pronounced (see below).

Finally, the influence of ocean loading via the sea level equation may be seen in Fig. 8. This figure shows the absolute value of the difference in present-day RSL when the ocean load is added (i.e. RSL from case 'SLEPW' minus that from case 'PW'). Including the ocean load adds about 10 m depth to Hudson Bay and 4 m depth to the Baltic Sea, each corresponding to about 25 per cent change. There is also a noticeable change along global coastlines due to the eustatic sea level change.

3.3 Effects of 3-D viscosity variations: a sensitivity study

The finite-element code CitcomSVE allows us to calculate the viscoelastic response of an Earth with 3-D viscosity structure. In this section and the next we use this ability to show that PGR observations are particularly sensitive to viscosity variations within certain regions of the underlying mantle.

In this section we use a simplified, idealized PGR model to map out the regions in the mantle where viscosity perturbations may affect surface uplift measurements. The loading is point-like in space (i.e. no ice or ocean loads), and simply has Heaviside (step function) time dependence. Because of the large number of 3-D calculations necessary, we omit the polar wander feedback for simplicity and speed. The earth model we consider first has a uniform mantle viscosity of 2×10^{21} Pa s, and a 100 km thick elastic lithosphere (other parameters are given in Table 1).

The point load is applied and maintained at the North Pole, while uplift (or subsidence) rates are recorded at angular distances of 0°, 10°, 20°, 30°, 40° and 50° away from the load—these will be called the observation points. We then introduce into the mantle a small block of high viscosity, 50 times greater than the background viscosity, with a size of 200 km vertically and 200 km in radius laterally. The location of this viscosity anomaly is allowed to roam throughout the mantle. For each case, with the viscosity anomaly at a certain location, we use CitcomSVE to compute the resulting deformation for 60 Maxwell times, and the resulting uplift rate versus time is recorded at the same six observation points. The uplift rate at a certain observation point is compared with the rate for a case without the viscosity anomaly by computing a difference between the two curves given by

$$\varepsilon = \frac{\int |u_{\rm i}(t) - u_{\rm a}(t)|\, dt}{\int |u_{\rm i}(t)|\, dt}, \tag{19}$$

where $u_{\rm i}$ is the isoviscous (no anomaly) uplift rate and $u_{\rm a}$ is the rate at the same observation point with a viscosity anomaly at a certain location in the mantle. The integral is over 60 Maxwell times ($\sim$27 kyr).

The results are displayed in Fig. 9 in a fashion intended to illustrate a 'sensitivity region' in the mantle. Each plot (a–f) has a particular configuration of loading point (shown by the arrow) and observation point (shown by the eye), and represents 120 separate 3-D calculations. The shade of a certain location in the mantle

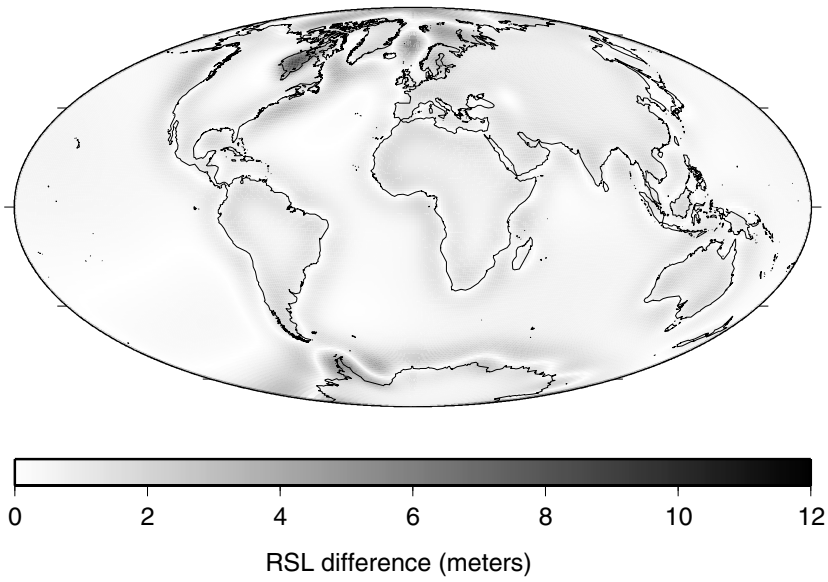

Figure 8. Influence of the ocean load, calculated by the sea level equation. Shown is the absolute value of the difference in present-day RSL between cases 'SLEPW' and 'PW'.

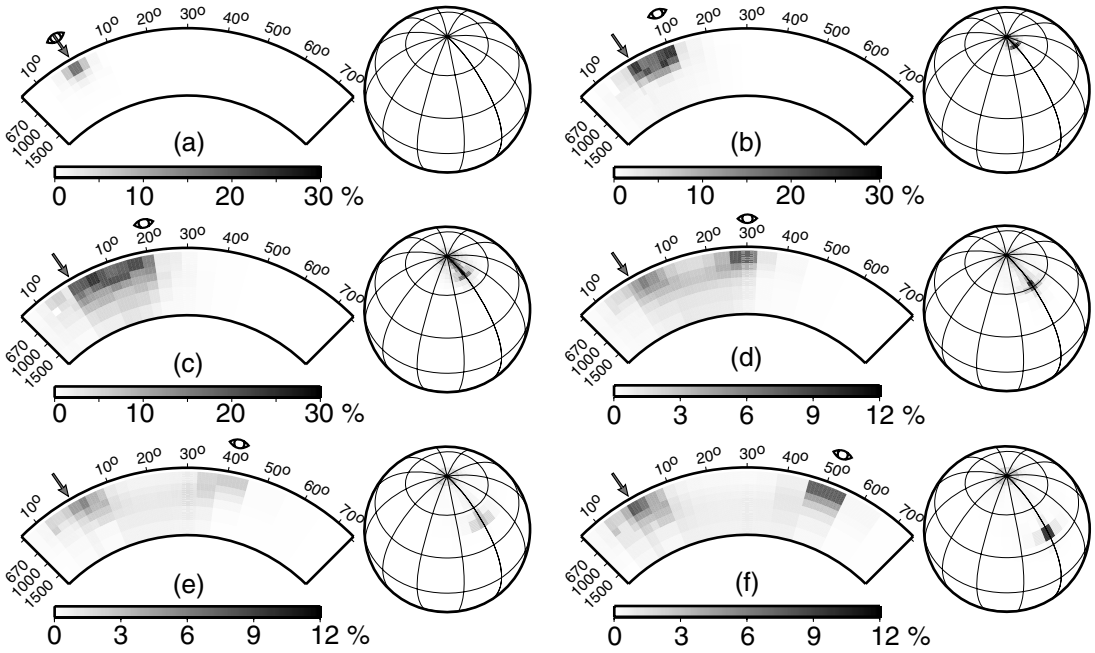

Figure 9. Illustration of the sensitivity of uplift rates to the location of a viscosity anomaly in the mantle. Each plot (a–f) has a particular configuration of load (arrow) and observation point (eye). The darkness of a certain location in the mantle for a given plot represents the difference in uplift rates (as measured by eq. 19) when a small high-viscosity anomaly is placed at that location, all else being unchanged. Beside each cross-section is shown the lateral structure of the sensitivity region at shallow depth.

represents the difference in uplift rates (recorded at the observation point, the eye symbol) when the small high-viscosity anomaly is placed at that location, everything else being unchanged. The values are computed by eq. (19), and expressed in per cent. Beside each cross-section is a surface plot of the sensitivity region at shallow depth, showing its lateral extent.

In each plot of Fig. 9 we see that PGR is particularly sensitive to viscosity structure both beneath the point of measured topography change and beneath the load. Even at great distances from the load (plot f), uplift rates are as sensitive to viscosity perturbations beneath the load as they are to local perturbations. These figures may be interpreted as identifying, with increased colouration, which regions of the mantle are 'sampled' when deformation is measured. They imply that if one infers a mantle viscosity from a measurement of PGR deformation (at least for the type of loading discussed here), one is only gaining knowledge of the viscosity within the sensitivity region shown. Although this is an idealized study of simple point-loading, and although the deformation is known to depend non-linearly on the configuration of an extended load, the sensitivity regions shown suggest a strong dependence on the viscosity immediately below the observation point as well as that beneath the load. The deformation rates also tend to 'sample' the viscosity structure between these two points, and to greater depth when the points are farther apart. This is particularly noticeable in plots (d) and (e), where the sensitivity region forms a sort of bridge between the points of greatest sensitivity, at the load and observation. It is also notable that there is virtually no sensitivity to viscosity perturbation outside of the corridor between these two points.

The same study was repeated with two variations. In the first, we used an anomaly with a viscosity 50 times *smaller* than the uniform background viscosity of 2×10^{21} Pa s. In the second, we used an anomaly also with 50× *greater* viscosity than background, but with a background viscosity consisting of two layers: 10^{22} Pa s in the lower mantle and 3×10^{20} Pa s in the upper mantle. In both variations, the sensitivity region of the mantle was not significantly different from that seen in Fig. 9.

3.4 Effects on PGR of realistic 3-D viscosity

In this section we approach the question of the influence of 3-D viscosity variations by comparing the PGR response of 1-D viscosity and 3-D viscosity derived from seismic models (Section 2.3). The 1-D structures are derived by averaging over lateral variations in the 3-D model. The intention is to compare methods of deriving a 1-D average from the 3-D structure to best reproduce the PGR observations from the 3-D model. If an optimal method exists, it could be used to describe how 1-D viscosity structures, derived from actual PGR observations, relate to the true 3-D viscosity of the Earth.

For this comparison, we force the Earth with the glacial load described in Section 2.1, and include the effects of polar wander feedback and ocean loading via the sea level equation. We study two 3-D viscosity models that differ only in that one is chosen to have a viscosity discontinuity at 670 km depth of about a factor of 30 (this is the model shown in Section 2.3) and the other has a factor of two discontinuity. These two models are derived identically, except for the choices for the values of A_0 in eq. (16). We concern ourselves first with the model having a factor of 30 viscosity jump.

From the 3-D model we derive a suite of 1-D models by laterally averaging the logarithm of the viscosity, subject to a weighting function $w(\theta, \varphi)$. The precise averaging procedure is described in Appendix B. We consider the four 1-D models discussed in Section 2.3 and shown in Fig. 3: a uniform 'global' average, a global 'ice-weighted' average, a local 'Hudson Bay' average and a local 'east coast' average.

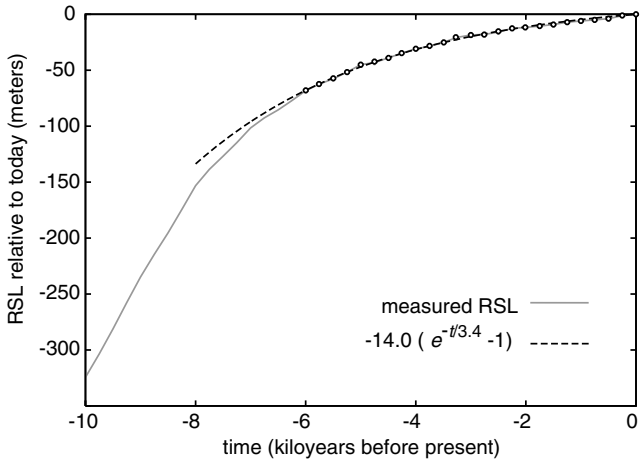

Figure 10. Illustration of the calculation of a relaxation time. The grey line is the RSL at Churchill, Canada (on the west shore of Hudson Bay) relative to its present-day value. Twenty-five samples of this curve (circles) are used to fit a function of the form $a[\exp(-t/T) - 1]$, where T is the relaxation time. The best fit to these points, at $a = -14.0$ m and $T = 3.4$ kyr, is shown as the dashed line.

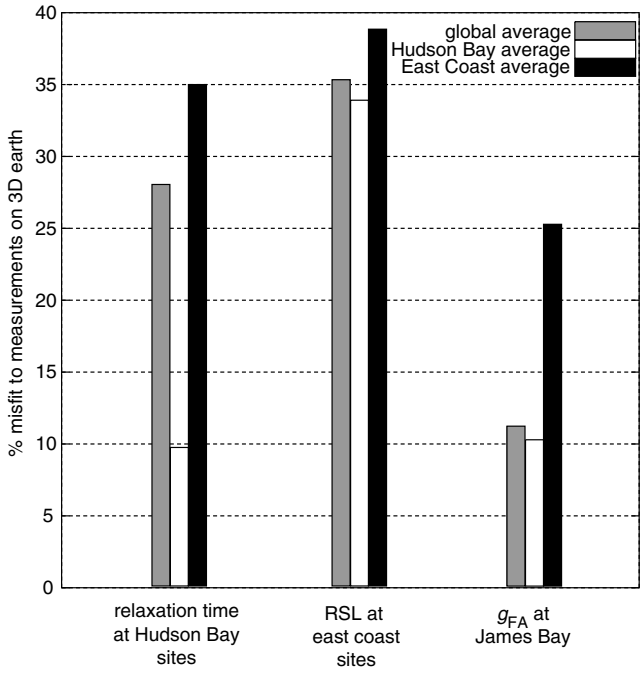

Figure 11. Per cent misfit between PGR observations from the 3-D earth model and those from three 1-D viscosity models: the global average (grey), the Hudson Bay average (white) and the east coast average (black). The three observation sets are relaxation times at several sites around Hudson Bay (left), RSL at several sites along the east coast of North America (centre) and the present-day free-air gravity anomaly over James Bay (right).

After computing the Earth's complete response for each model (using CitcomSVE and the spectral method for the 3-D and 1-D models, respectively), we record several PGR-related phenomena for comparison. These include 'relaxation times' for several sites around Hudson Bay, computed from the time dependence of relative sea level (RSL) over the last 6 kyr (i.e. since the disappearance of the Laurentide ice sheet). The relaxation time T is computed by fitting a curve of the form $a[\exp(-t/T) - 1]$ to 25 points of the RSL relative to today over the last 6 kyr (i.e. we find the values a and T that minimize the χ^2 residual for the sampled RSL points). This is demonstrated in Fig. 10. For several sites along the east coast of North America we consider RSL histories over the last 6 kyr, relative to the present day. We cannot use relaxation times at these sites because the deformation is not even approximately exponential in time. We also record the maximum present-day free-air gravity anomaly, g_{FA}, which occurs near James Bay at the southern end of Hudson Bay. These results, relaxation times, RSL curves and g_{FA}, may all be considered local to the Laurentide region. In addition, we consider three measurements of *global* present-day PGR: $\dot{J}_2$, the rate of true polar wander and the rate of change of higher-order gravity Stokes coefficients (data anticipated from the GRACE mission). It should be mentioned that although these quantities have been interpreted as PGR signals in previous studies, there is some ambiguity in their interpretation; for our models, however, their change is due entirely to PGR.

We use these data as follows. For a given 1-D model, for each PGR observation, we compute a misfit to the corresponding result from the 3-D Earth. In the case of the east coast RSL curves, the misfit is the difference measured by eq. (19), where $u(t)$ is taken to mean the RSL relative to today, and the integral is over the last 6 kyr. The RSL misfits are then combined by rms average. In the case of the GRACE Stokes coefficients, the per cent difference is computed for each coefficient up to spherical harmonic degree 10, and then averaged together, being weighted by the reciprocal of the estimated errors on the GRACE C_l^m, S_l^m coefficients (Velicogna *et al.* 2005). For the remaining PGR observations that are simply scalars, the misfit is just the per cent difference in the absolute value of the result.

In computing these misfits, we are interested in which 1-D model can best reproduce the PGR of the 3-D model. First we consider how the two local viscosity models (the 'Hudson Bay' average and the 'east coast' average) reproduce the local PGR observations (relaxation times at the Hudson Bay sites, RSL at the east coast sites and g_{FA} over James Bay). Fig. 11 shows the misfit of the 1-D results to the 'true' (synthetic) data from the 3-D Earth. The results of the global average 1-D model are also included for comparison. The model that best reproduces the 3-D results overall is the one taken from Hudson Bay (white bars). This echoes an observation of the previous section that topography change is sensitive to the viscosity under the loading, even when it is distant from the loaded region. Measurements of RSL along the east coast, which is somewhat removed from the ice-loaded region, turn out to be difficult to reproduce with any of these 1-D viscosity models. This may be due to the sensitivity of these RSL measurements to both of the rather different 1-D structures: the local 'east coast' structure as well as the 'Hudson Bay' (beneath load) structure. Relaxation times around Hudson Bay and g_{FA} at James Bay are both best reproduced with the local viscosity structure.

In an expanded search for 1-D models that might reproduce the east coast RSL data from the 3-D Earth, we also consider a variety of weighting functions $w(\theta, \varphi)$ including combining Hudson Bay and east coast viscosity structures, or using a broader or narrower region over which to average. We find, however, that none of the 1-D models can reproduce the east coast RSL of the 3-D Earth significantly better than the misfits shown in Fig. 11.

To consider the global measures of PGR (present-day $\dot{J}_2$, polar wander rate and GRACE gravity coefficients), we compare the global average viscosity and the ice-weighted viscosity. The misfits of the 1-D model results to those from the 3-D Earth are shown

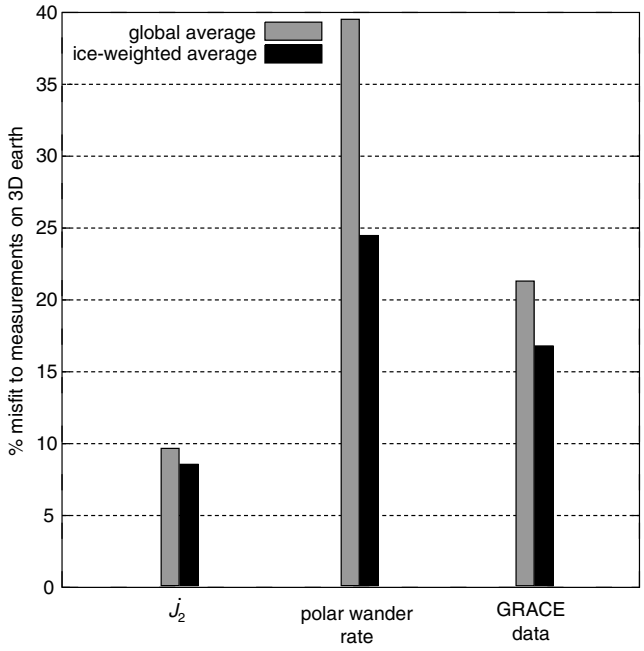

Figure 12. Per cent misfit between PGR observations from the 3-D earth model and those from two 1-D viscosity models: the global average (grey) and the ice-weighted average (black). The three observations are present-day $\dot{J}_2$ (left), polar wander rate (centre) and GRACE gravity coefficients (right).

in Fig. 12. For each observation, the ice-weighted average is closer to the 3-D result than the global average. This is again reminiscent of a conclusion of the previous section: that the viscosity structure beneath the loading will affect PGR everywhere. In this case there is no localized point of measurement since these observables are all global in scale, thus the viscosity beneath all the ice-loaded regions of the Earth contributes most to the result.

The results in Fig. 12 for the polar wander rate show rather large misfits and unusually large sensitivity to differences between the 1-D models. However, this is mostly due to a coincidence of this particular 3-D model, which has the polar wander rate crossing zero at nearly the present day—this makes comparisons of per cent difference rather less stable. This difficulty is removed if we consider a slightly different viscosity structure, without this coincidental zero crossing at the present day, which we consider next.

As mentioned earlier, we have also created a different 3-D viscosity model with a factor of two viscosity discontinuity at the 670 km discontinuity. The experiment is repeated with this 3-D model and with the same 1-D averages derived from it. Comparing the PGR results as before, the conclusions drawn above remain the same. We find again that the viscosity beneath Laurentia best reproduced the Hudson Bay data and g_{FA}, while east coast RSL was difficult to obtain with our 1-D structures. Also, the 1-D structure derived from an ice-weighted average reproduced all global measures of PGR better than a full global average. The misfit values shown in Figs 11 and 12 are similar for this case, except for the polar wander rates. In the case of the polar wander calculations, the global average has a 17.8 per cent misfit and the ice-weighted average has a 16.3 per cent misfit.

It is notable that, despite substantial variations in upper mantle viscosity and lithospheric thickness (Fig. 3), most of the misfits discussed above and shown in Figs 11 and 12 do not differ greatly from each other—an important exception being the comparison of relaxation times at Hudson Bay. This is not for lack of variety in the production of 1-D models, as many different weighting functions were considered in producing 1-D averages (with similar results). Further, it appears that the 1-D models, in general, have difficulty reproducing the PGR results of the 3-D viscosity model to better than about 10 per cent. This suggests that a significant contribution to the misfit values may be due to the complicating effects of the 3-D viscosity structure. A similar sensitivity (to lithospheric and asthenospheric lateral variations) was also noted by Martinec *et al.* (2001). Only when the most local features of the 3-D model are being probed, by making local observations in the previously loaded region, is there an unambiguously preferred 1-D viscosity structure.

4 DISCUSSION AND CONCLUSION

We have used two complementary methods to solve the forward problem of glacial isostatic adjustment: a spectral method for strictly 1-D (spherically symmetric) earth models and a finite-element method for models with 3-D viscosity structure. We have augmented both methods by implementing three additional effects: solution for the response at spherical harmonic degree one (or centre of mass motion), a gravitationally self-consistent ocean load via the sea level equation, and the influence of polar wander feedback. Each of these effects is found to have a significant influence on PGR observables such as relative sea level. The strength of the degree-one signal is of the same order of magnitude as the other longest wavelengths. Application of an ocean load significantly changes sea levels, especially in regions of marine-based ice sheets. The feedback of polar wander upon potential and deformation substantially changes the signal at spherical harmonic degree two, order ± 1, and may influence other harmonics if a coupling mechanism exists (though by less than 2 per cent).

With all these effects implemented in both the finite-element and the spectral methods, the two methods were benchmarked against each other, differing in global topography and geoid by typically less than 2 per cent.

We also examined the influence of lateral viscosity variations upon measurements of post-glacial rebound in two ways. First, we used a simplified, idealized PGR model to map out the regions in the mantle where viscosity perturbations may affect surface uplift measurements. One may think of this as a 'sensitivity region,' describing where in the mantle the deformation measurement is sensitive to viscosity perturbations. The regions of greatest sensitivity are beneath the loading and beneath the point of measurement. The sensitivity region generally extends in a corridor between these two points and disappears rapidly outside it.

As a second approach to study the influence of lateral viscosity variations, we constructed a realistic 3-D viscosity model from seismic tomography models. We recorded the resulting PGR observables such as relaxation times, relative sea level, gravity and polar wander rate, and compared them with similar observations on a 1-D (spherically symmetric) viscosity model that was derived from a suitable average of the 3-D structure. We found results that corresponded consistently with our conclusions from the sensitivity study. Namely, that PGR observations tend to depend on the viscosity structure beneath the ice load, whether or not the observation is made there. For observations made at the same location as the loading, such as the relaxation time of the uplift of Hudson Bay, results of the 3-D model agreed well with a 1-D model whose viscosity was that beneath Hudson Bay. This suggests that local observations at the loaded region can give information about the local viscosity structure. Global PGR measurements ($\dot{J}_2$, polar wander rate and

GRACE gravity coefficients) for which there is no 'local' region, tend to reflect the viscosity structure beneath the ice-loaded regions of the Earth. These results suggest that a 1-D viscosity structure derived from global PGR observations will most closely resemble not a global lateral average of the Earth's viscosity, but an average that heavily weights the viscosity structure beneath the loaded region. For local PGR observations away from the loading (sea levels along the North American east coast) none of our 1-D models could reproduce well the results of the calculation with 3-D viscosity. In this case, PGR is sensitive to both the local viscosity structure and the substantially different structure beneath the loaded regions. The nature of this problem is *essentially* 3-D, so we cannot expect similar deformation from any 1-D viscosity model. Finally, for all cases except those where local observations are made at the location of the loading, 1-D models have difficulty reproducing the PGR observations of the 3-D viscosity model—further evidence of the influence of lateral viscosity variations in these PGR data.

ACKNOWLEDGMENTS

This research is supported by NSF grant EAR-0087567, and by a grant from the David and Lucile Packard Foundation. We thank N. Shapiro and A. McNamara for their contributions to the creation of the 3-D viscosity model.

REFERENCES

Bills, B.G. & James, T.S., 1997. Polar motion of a viscoelastic earth due to glacial cycle mass loading, *Geophys. J. Int.,* **102**(B4), 7579–7602.

Farrell, W.E., 1972. Deformation of the earth by surface loads, *Rev. Geophys. Space Phys.*, **10,** 761–797.

Farrell, W.E. & Clark, J.A., 1976. On postglacial sea level, *Geophys. J. R. astr. Soc.*, **46,** 647–667.

Han, D. & Wahr, J., 1989. Post-glacial rebound analysis for a rotating earth, in *Slow Deformations and Transmission of Stress in the Earth*, American Geophysical Union Geophysical Monograph 49, eds Cohen, S. & Vanicek, P., pp. 1–6, American Geophysical Union, Washington, DC.

Karato, S., 1993. Importance of anelasticity in the interpretation of seismic tomography, *Geophys. Res. Lett.*, **20,** 1623–1626.

Kaufmann, G., Wu, P. & Guoying, L., 2000. Glacial isostatic adjustment in Fennoscandia for a laterally heterogeneous earth, *Geophys. J. Int.*, **143**(1), 262–273.

Kendall, R.A., Mitrovica, J.X. & Milne, G.A., 2005. On post-glacial sea level – II. Numerical formulation and comparative results on spherically symmetric models, *Geophys. J. Int.,* **161,** 679–706.

Lambeck, K., 1980. *The Earth's Variable Rotation: Geophysical Causes and Consequences*, Cambridge University Press, Cambridge.

Martinec, Z., Cadek, O. & Fleitout, L., 2001. Can the 1D viscosity profiles inferred from postglacial rebound data be affected by lateral viscosity variations in the tectosphere?, *Geophys. Res. Lett.*, **23,** 4403–4406.

McNamara, A.K., van Keken, P.E. & Karato, S., 2003. Development of finite strain in the convecting lower mantle and its implications for seismic anisotropy, *J. geophys. Res.*, **108**(B5), 2230.

Milne, G.A., Mitrovica, J.X. & Davis, J.L., 1999. Near-field hydro-isostasy: the implementation of a revised sea-level equation, *Geophys. J. Int.*, **139,** 464–482.

Mitrovica, J.X., 2003. Recent controversies in predicting post-glacial sea-level change, *Quatern. Sci. Rev.*, **22**(2–4), 127–133.

Mitrovica, J.X. & Peltier, W.R., 1992. A comparison of methods for the inversion of viscoelastic relaxation spectra, *Geophys. J. Int.*, **108,** 410–414.

Mitrovica, J.X., Wahr, J., Matsuyama, I. & Paulson, A., 2005. The rotational stability of an ice age Earth, *Geophys. J. Int.*. doi: 10.1111/j.1365-246X.2005.02609.x.

Munk, W.H. & MacDonald, G.J.F., 1960. *The Rotation of the Earth*, Cambridge University Press, New York.

Ritsema, J., van Heijst, J.H. & Woodhouse, J.H., 1999. Complex shear wave velocity structure imaged beneath Africa and Iceland, *Science*, **286,** 1925–1928.

Shapiro, N. & Ritzwoller, M., 2002. Monte-Carlo inversion for a global shear velocity model of the crust and upper mantle, *Geophys. J. Int.*, **151**(1), 88–105.

Shapiro, N. & Ritzwoller, M., 2004. Thermodynamic constraints on seismic inversions, *Geophys. J. Int.*, **157**(3), 1175–1188.

Tushingham, A.M. & Peltier, W.R., 1991. ICE-3G: a new global model of Late Pleistocene deglaciation based upon geophysical predictions of post-glacial relative sea level change, *J. geophys. Res.*, **70**(B3), 4497–4523.

van der Lee, S., 2002. High-resolution estimates of lithospheric thickness from Missouri to Massachusetts, USA, *Earth planet. Sci. Lett.*, **203**(1), 15–23.

Velicogna, I.J., Wahr, J., Hanna, E. & Huybrechts, P., 2005. Short term mass variability in Greenland, from GRACE, *Geophys. Res. Lett.,* **32,** in press.

Wahr, J., van Dam, T., Larson, K. & Francis, O., 2001. Geodetic measurements in Greenland and their implications, *J. geophys. Res.*, **106**(B8), 16567–16582.

Wu, P. & Peltier, W.R., 1982. Viscous gravitational relaxation, *Geophys. J. R. astr. Soc.*, **70,** 435–485.

Wu, P. & Peltier, W.R., 1984. Pleistocene deglaciation and the Earth's rotation: a new analysis, *Geophys. J. R. astr. Soc.*, **76,** 753–792.

Wu, P. & van der Wal, W., 2003. Postglacial sealevels on a spherical, self-gravitating viscoelastic earth: effects of lateral viscosity variations in the upper mantle on the inference of viscosity contrasts in the lower mantle, *Earth planet. Sci. Lett.*, **211**(1), 57–68.

Yamazaki, D. & Karato, S., 2001. Some mineral physics constraints on the rheology and geothermal structure of the earth's lower mantle, *Am. Mineral.*, **86,** 385–391.

Zhong, S., Zuber, M.T., Moresi, L. & Gurnis, M., 2000. Role of temperature-dependent viscosity and surface plates in spherical shell models of mantle convection, *J. geophys. Res.*, **105**(B5), 11063–11082.

Zhong, S., Paulson, A. & Wahr, J., 2003. Three-dimensional finite-element modelling of earth's viscoelastic deformation: effects of lateral variations in lithospheric thickness, *Geophys. J. Int.*, **155**(2), 679–695.

APPENDIX A: DETAILED PROCEDURE FOR DERIVATION OF THE 3-D VISCOSITY MODEL

The detailed procedure for deriving the 3-D viscosity model is given here. The seismic tomography models used are the following: S20RTS (Ritsema *et al.* 1999) gives global shear velocity perturbations relative to PREM; NA00 van der Lee (2002) gives absolute shear wave velocities down to 670 km and Moho depth beneath North America; CUB2.0 (Shapiro & Ritzwoller 2002) provides a 1-D velocity structure down to 400 km depth. We distinguish between 3-D and 1-D (radially dependent) functions by showing the dependent variable as **r** and *r*, respectively.

(1) Set the global shear wave velocity structure. For conversion purposes, we need absolute shear wave velocities, V_s (**r**), above 400 km depth, and velocity perturbations, $(\delta V_s/V_s)(\mathbf{r})$, below 400 km.

(a) Get global velocity perturbations, $(\delta V_s/V_s)(\mathbf{r})$, from the model S20RTS. Above 400 km, add the 1-D velocity structure (provided by CUB2.0) to obtain absolute shear wave velocity, V_s (**r**).

(b) Use the higher-resolution NA00 velocity model under North America. For regions within the NA00 model domain but below 400 km depth, convert the NA00 absolute velocity to velocity perturbation $(\delta V_s/V_s)(\mathbf{r})$ using the NA00 average.

(2) Convert velocities to temperature, $T(\mathbf{r})$.

(a) Above 400 km depth, directly convert $V_s\ (\mathbf{r}) \rightarrow T(\mathbf{r})$, based on laboratory-measured material properties. We use the method of Shapiro & Ritzwoller (2004).
(b) Below 400 km, use a proportionality constant of 0.3 to convert velocity perturbation to density perturbation (Karato 1993): $(\delta\rho/\rho)(\mathbf{r}) = (0.3\delta V_s/V_s)(\mathbf{r})$. Divide this by a depth-dependent thermal expansivity, $\alpha(r)$, to obtain temperature variations, $\delta T(\mathbf{r})$. We use $\alpha(r) = [r' + 3(1 - r')] \times 10^{-5}$, where the depth $r' = r/r_{\rm b}$ where $r_{\rm b}$ is the depth of the CMB. To the temperature variations, add the 1-D adiabatic temperature for a 3-D temperature field: $T(\mathbf{r}) = T_{\rm ad}\ (r) + \delta T(\mathbf{r})$.

(3) Convert temperature to viscosity, $\eta(\mathbf{r})$.

(a) Obtain a depth-dependent melting temperature, $T_{\rm m}(r)$. We use $T_{\rm m}(r) = 2100 + 1.4848r - (5 \times 10^{-4}\ r^2)$ in the upper mantle, and $T_{\rm m}(r) = 2916 + 1.25r - (1.65 \times 10^{-4}\ r^2)$ in the lower mantle, where r is the depth in kilometres (Yamazaki & Karato 2001) (as used in McNamara *et al.* 2003).
(b) Use the relation $\eta(\mathbf{r}) = A_0 \exp[\gamma T_{\rm m}\ (r)/T(\mathbf{r})]$, with $\gamma = 17$ in the upper mantle and $\gamma = 10$ in the lower mantle (Yamazaki & Karato 2001) (as used in McNamara *et al.* 2003). The leading constant A_0 is chosen for the upper and lower mantle to roughly set the magnitudes there. For the case shown in Fig. 2, we use $A_0 = 2 \times 10^9$ Pa s in the upper mantle and $A_0 = 1.2 \times 10^{13}$ Pa s in the lower mantle. For comparison, we also consider a case with $A_0 = 2 \times 10^{12}$ Pa s in the lower mantle, giving about a factor of 2 viscosity discontinuity at 670 km depth.

(4) Set the elastic lithosphere thickness, $T_{\rm e}\ (\theta, \varphi)$.

(a) Assemble a reasonable model of elastic thickness from studies of loading and heat flux. We use the model discussed in Zhong *et al.* (2003, section 5.1).
(b) Set viscosity within the lithosphere to 10^{25} Pa s.

APPENDIX B: COMPUTING AVERAGE VISCOSITY

Starting with a 3-D viscosity structure, $\eta_3\ (\theta, \varphi, r)$, and a weighting function $w(\theta, \varphi)$, we perform a lateral average of viscosity to obtain a 1-D, spherically symmetric structure, $\eta_1(r)$. This is accomplished as follows:

(1) Define the effective (elastic) lithospheric thickness $T_{\rm e}(\theta, \varphi)$ by the depth at which the viscosity η_3 falls below a chosen cut-off value (we use 10^{25} Pa s).

(2) Find the average lithospheric thickness, weighted appropriately: $\langle T_{\rm e}\rangle = \int w T_{\rm e}\, d\Omega / \int w\, d\Omega$. Set the 1-D viscosity above this radius to a be very high: $\eta_1(r) = 10^{25}$ Pa s for depths $< \langle T_{\rm e}\rangle$.

(3) At each depth specified by the 3-D viscosity model, we find the weighted average of the logarithm of the viscosity in all non-lithospheric regions. The non-lithospheric region, $\mathcal{N}$, is defined by those regions at the specified depth with viscosity less than the chosen elastic cut-off (10^{25} Pa s). For depths greater than $\langle T_{\rm e}\rangle$, the 1-D viscosity is given by

$$\eta_1(r) = \exp\left(\frac{\int_{\mathcal{N}} w \ln \eta_3\, d\Omega}{\int_{\mathcal{N}} w\, d\Omega}\right) \qquad \text{for depths } > \langle T_{\rm e}\rangle\,.$$